

Title: Uncertainty in solar wind forcing explains polar cap potential saturation

Authors: Nithin Sivadas^{1,2*}, David Sibeck², Varsha Subramanyan³, Maria-Theresia Walach⁴, Kyle Murphy⁵ and Alexa Halford⁶

Affiliations:

¹Department of Physics, The Catholic University of America, Washington, D.C., USA

²Space Weather Laboratory, NASA Goddard Space Flight Center, Greenbelt, Maryland, USA

³Department of Physics, University of Illinois Urbana-Champaign, USA

⁴Department of Physics, Lancaster University, United Kingdom

⁵Independent Contractor, Thunder Bay, Ontario, Canada

⁶ITM Physics Laboratory, NASA Goddard Space Flight Center, Greenbelt, Maryland, USA

*Corresponding author. Email: nithin@bu.edu

Abstract: Extreme space weather events occur during intervals of strong solar wind electric fields. Curiously during these intervals, their impact on measures of the Earth's response, like the polar cap index, is not as high as expected. Theorists have put forward a host of explanations for this saturation effect, but there is no consensus. Here we show that the saturation is *merely a perception* created by uncertainty in the solar wind measurements, especially in the measurement times. Correcting for the uncertainty reveals that extreme space weather events elicit a ~300% larger impact than previously thought. Furthermore, they point to a surprisingly general result relevant to any correlation study: uncertainty in the measurement time can cause a system's linear response to be perceived as non-linear.

One-Sentence Summary: Uncertainty in measurement times can cause a system's linear response to be misinterpreted as non-linear.

In the past four decades, theorists have put forward at least nine models for the saturation of the polar cap index (4, 5, 7). The models explain the saturation by either reduced energy transfer from the solar wind or reduced plasma convection in the ionosphere during high solar wind electric field values. None of these explanations have been confirmed by direct observational evidence (5).

This paper proposes a very different explanation for the saturation effect: uncertainty in the input measurements. Correcting for the uncertainty shows that the true magnetosphere response is linear over the full range of solar wind input—implying that the impact of extreme space weather is vastly higher than previously assumed. Finally, we demonstrate that uncertainty in measurement times can lead to a system's linear response being misunderstood as non-linear. The importance of this work goes beyond Heliophysics, as it is relevant to any correlation study between a measure of the system's forcing and its response.

There is always an inherent error in the input solar wind reconnection electric field values mapped down to the polar ionosphere ($\hat{E}_m^* \neq \hat{E}_m$). The solar wind monitors are located far upstream from Earth. Hence, there are random errors in our calculations of the times when the solar wind reaches the Earth. The nature of the error stems from the following facts: 1) There are random errors in the estimates of the solar wind propagation times from the L1 liberation point, where it is measured, down to the ionosphere, 2) The random errors need not be the same across time or solar wind fluxes, 3) The reconnection electric field is log-normally distributed (See Fig. S1) (8).

Such errors in input measurements mean that the magnetospheric response to stronger electric fields is likely to be associated with that of the smaller and more typical electric fields. It is essentially an effect associated with a reversion towards the mean (9). The reversion becomes more acute the greater the solar wind electric field, hence the saturation effect. In other words, the random error in the stochastic solar wind forcing leads to a non-linear bias in the regression function of its magnetosphere response. Here, the regression function $\langle E_{PC} | \hat{E}_m^* \rangle$ is the conditional expectation of the polar cap index (E_{PC}) for a given estimate of the solar wind reconnection electric field value (\hat{E}_m^*) mapped to the polar ionosphere. The cause of the non-linear bias is the uncorrected use of \hat{E}_m^* —the erroneous estimate of the reconnection electric field mapped to the ionosphere as a covariate instead of its true value \hat{E}_m .

We demonstrate this through a Monte-Carlo solution of a statistical error model that considers the uncertainty in the solar wind propagation time and its magnitude (10). The non-linear regression function calculated by the model coincides with the saturation of the polar cap potential observed in data (See Fig. 2). Given the uncertainties in the solar wind propagation from L1 to the polar cap, we should expect the polar cap potential to saturate with the erroneous estimate of the solar wind reconnection electric field.

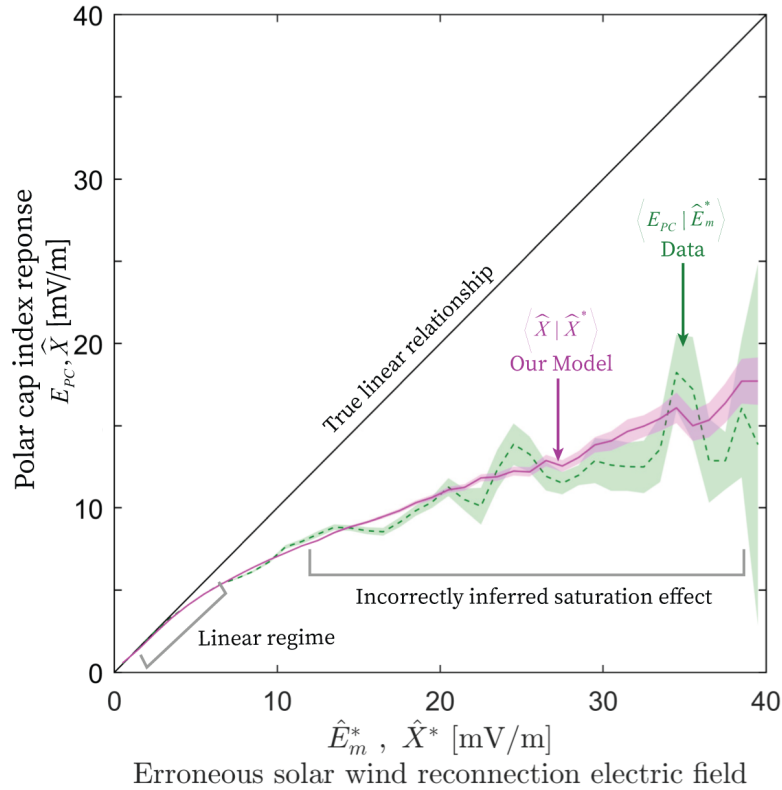


Fig. 2. Our model reproduces the observed saturation polar cap index extremely well. The green dashed lines show the polar cap index saturation data observed for a given erroneous estimate of the solar wind reconnection electric field \hat{E}_m^* derived from the literature. The data is an average of measurements over 20 years. The solid magenta line results from the statistical model we developed based on the uncertainties in solar wind measurements.

Our work shows that the true magnetosphere response is linear over the full range of solar wind input—but the saturation effect increases as uncertainties in the solar wind input increase (See Fig. 3A). There is no need to invoke new physics for the solar wind-magnetosphere interaction: the saturation effect is entirely the result of uncertainties in the solar wind measurements and its arrival time. Using regression calibration of the erroneous estimate (\hat{E}_m^c), we remove the non-linear bias in the regression function (I). The new regression function calculated using the corrected reconnection electric field data $\langle E_{PC} | \hat{E}_m^c \rangle$ is largely linear. Strengthening this finding is the behavior of an independently measured and alternate ionosphere parameter - the auroral electrojet current strength (SML). The electrojet strength increases linearly with the corrected solar wind field (See Fig. 3B).

The linearity implies that the actual effect of extreme space weather on Earth might be much higher than previously thought. At around 40 mV/m reconnection electric field, the effect on the polar cap index is $\sim 300\%$ more than when we erroneously infer the saturated response. These results, finally, explain the decades-old question of polar cap potential saturation as a consequence of neglecting uncertainty in the estimates of solar wind propagation.

Correcting error in solar wind measurements reveals:

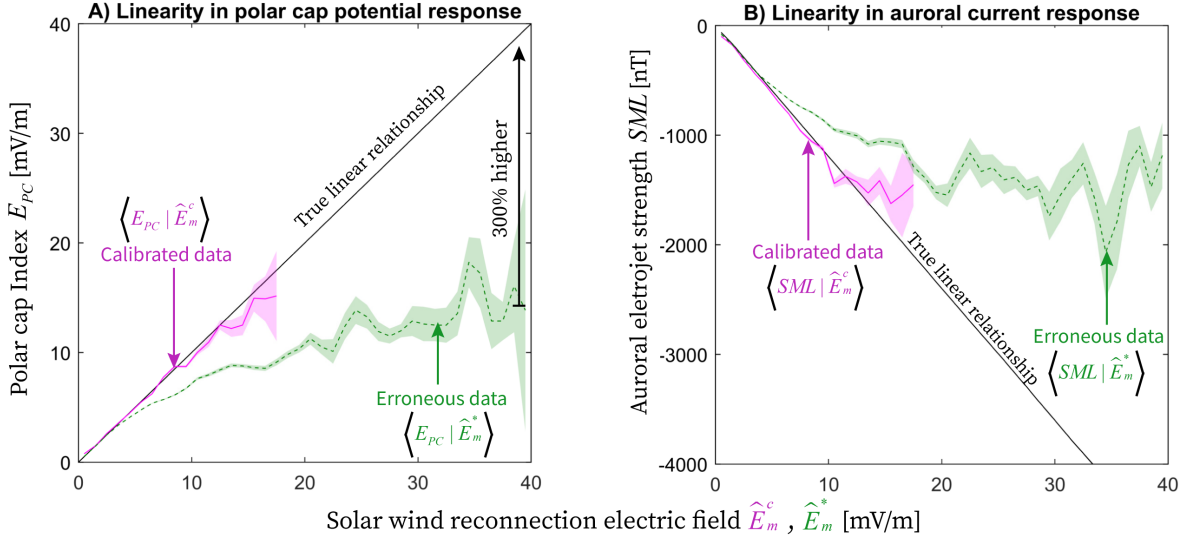


Fig. 3. The magnetospheric response is linear with solar wind driving after calibrating the uncertainty. A) Regression calibration of the solar wind reconnection electric field estimate leads to a linear ionospheric response. The green dashed lines show the polar cap index saturation data observed for a given erroneous estimate of the solar wind reconnection electric field described in the literature $\langle E_{PC} | \hat{E}_m^* \rangle$. The solid magenta line is the true relationship revealed after regression calibration $\langle E_{PC} | \hat{E}_m^c \rangle$. The linearity of the true response implies that at 40 mV/m of the solar wind reconnection field, the polar cap index response is $\sim 300\%$ greater than if the response were to saturate. B) The response of the auroral electrojet strength (SML), measured using an independent set of instruments in the ionosphere, also varies linearly with the calibrated reconnection electric field.

The importance of this result goes beyond space physics, as it is relevant to any correlation study. When the input is uncertain, we cannot directly extract the system's response to unusually large or small input values. Using analytic methods, we show that uncertainty in the time of input measurement can produce a perception of non-linearity in the response. The non-linear effect becomes more significant with increasing uncertainty of measurement times (See Fig. 4). In other words, temporal uncertainty in the input to a regression problem can bias the system's correlation response or regression function. The bias is non-linear if the input is a lognormal stochastic process. We demonstrate for the first time that this non-linear bias increases as a function of the ratio of the standard deviation of temporal uncertainty (σ_δ) and the autocorrelation time constant (κ) of the process (See Fig. 4). Lognormal processes are common in nature, as they are the limiting distribution of products of independently distributed random numbers(11–13). Hence this non-linear bias might be more common-place than we realize.

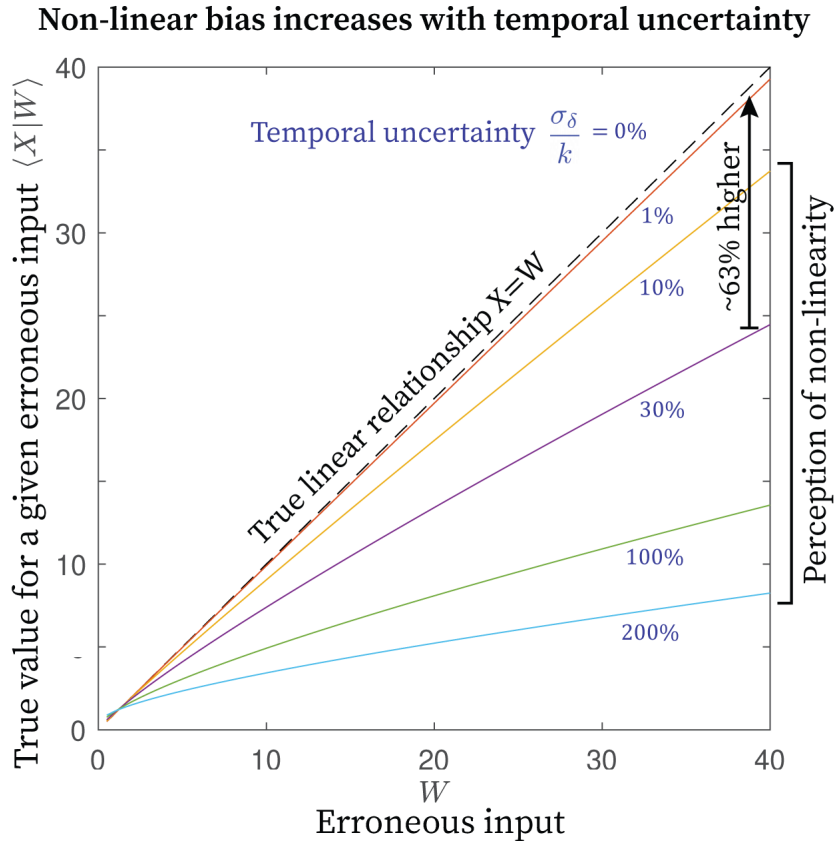


Fig. 4. Increasing temporal uncertainty leads to non-linearity in the regression function that is otherwise linear. X is a lognormal stochastic process with an autocorrelation time constant κ . W is an erroneous estimate of X , where the error comes from a temporal uncertainty $t + \delta$ with a standard deviation of σ_δ . The regression function $\langle X|W \rangle$ has a non-linear bias that increases with the ratio of the standard deviation of temporal uncertainty to the autocorrelation time constant (σ_δ/κ). When this ratio is 30%, the true regression function is at least $\sim 63\%$ higher than the biased regression function at the highest value of the erroneous input ($W = 40$ units).

Our findings have three main implications. First, it forces us to rethink the physics-based explanations of polar cap potential saturation developed in the last four decades and address the uncertainty in solar wind propagation. Second, the magnetospheric response to solar wind forcing is linear, implying that extreme space weather events can have a vastly higher impact on the Earth than if the response were to saturate. Finally, the temporal uncertainty in forcing can alter our interpretation of the response of forced systems, e.g., mistaking a linear system response to be non-linear. If the uncertainty is reduced or statistically corrected, it is possible to retrieve the true system response. This effect may be relevant to fields with rare events and uncertainty in input measurement times, such as seismology, astronomy, climate science, or medical diagnosis. It is also likely consequential to data analysis frameworks when used to make inferences of a system's behavior, such as non-linear error analysis, regression analysis, non-linear dynamics of delay systems, and machine learning.

References and Notes

1. J. P. Eastwood, E. Biffis, M. A. Hapgood, L. Green, M. M. Bisi, R. D. Bentley, R. Wicks, L.-A. McKinnell, M. Gibbs, C. Burnett, The Economic Impact of Space Weather: Where Do We Stand? *Risk Anal.* **37**, 206–218 (2017).
2. National Research Council, *Severe Space Weather Events: Understanding Societal and Economic Impacts: A Workshop Report*. (National Academies Press, Washington, DC, 2008; <https://doi.org/10.17226/12507>).
3. W. D. Gonzalez, B. T. Tsurutani, A. L. C. Gonzalez, E. J. Smith, F. Tang, S.-I. Akasofu, Solar wind-magnetosphere coupling during intense magnetic storms (1978-1979). *J. Geophys. Res. Sp. Phys.* **94**, 8835–8851 (1989).
4. J. E. Borovsky, B. Lavraud, M. M. Kuznetsova, *J. Geophys. Res. Sp. Phys.*, in press, doi:10.1029/2009JA014058.
5. S. G. Shepherd, Polar cap potential saturation: Observations, theory, and modeling. *J. Atmos. Solar-Terrestrial Phys.* **69**, 234–248 (2007).
6. P. Stauning, The polar cap (PC) index combination, PCC: Relations to solar wind properties and global magnetic disturbances. *J. Sp. Weather Sp. Clim.* **11**, 19 (2021).
7. G. Siscoe, J. Raeder, A. J. Ridley, Transpolar potential saturation models compared. *J. Geophys. Res. Sp. Phys.* **109**, 9203 (2004).
8. I. S. Veselovsky, A. V. Dmitriev, A. V. Suvorova, Lognormal, Normal and Other Distributions Produced by Algebraic Operations in the Solar Wind. *AIP Conf. Proc.* **1216**, 152 (2010).
9. A. G. Barnett, J. C. van der Pols, A. J. Dobson, Regression to the mean: what it is and how to deal with it. *Int. J. Epidemiol.* **34**, 215–220 (2005).
10. Materials and methods are available as supplementary materials at the Science website.
11. W. H. Campbell, Geomagnetic storms, the Dst ring-current myth and lognormal distributions. *J. Atmos. Terr. Phys.* **58**, 1171–1187 (1996).
12. J. H. GADDUM, Lognormal Distributions. *Nat. 1945 1563964.* **156**, 463–466 (1945).
13. J. Aitchison, J. A. C. Brown, *The Lognormal distribution* (University Press, United Kingdom, 1969).
14. R. P. Lepping, M. H. Acuña, L. F. Burlaga, W. M. Farrell, J. A. Slavin, K. H. Schatten, F. Mariani, N. F. Ness, F. M. Neubauer, Y. C. Whang, J. B. Byrnes, R. S. Kennon, P. V. Panetta, J. Scheifele, E. M. Worley, The WIND magnetic field investigation. *Sp. Sci. Rev. 1995 711.* **71**, 207–229 (1995).
15. J. R. Kan, L. C. Lee, Energy coupling function and solar wind-magnetosphere dynamo. *Geophys. Res. Lett.* **6**, 577–580 (1979).
16. M. A. Doyle, W. J. Burke, S3-2 measurements of the polar cap potential. *J. Geophys. Res. Sp. Phys.* **88**, 9125–9133 (1983).
17. J. H. King, N. E. Papitashvili, Solar wind spatial scales in and comparisons of hourly Wind and ACE plasma and magnetic field data. *J. Geophys. Res. Sp. Phys.* **110**, 2104 (2005).

18. D. R. Weimer, D. M. Ober, N. C. Maynard, M. R. Collier, D. J. McComas, N. F. Ness, C. W. Smith, J. Watermann, Predicting interplanetary magnetic field (IMF) propagation delay times using the minimum variance technique. *J. Geophys. Res. Sp. Phys.* **108**, 1026 (2003).
19. S. Haaland, G. Paschmann, B. U. Ö. Sonnerup, Comment on “A new interpretation of Weimer et al.’s solar wind propagation delay technique” by Bargatze et al. *J. Geophys. Res. Sp. Phys.* **111**, 6102 (2006).
20. T. Knetter, F. M. Neubauer, T. Horbury, A. Balogh, Four-point discontinuity observations using Cluster magnetic field data: A statistical survey. *J. Geophys. Res. Sp. Phys.* **109**, 6102 (2004).
21. O. A. Troshichev, A. S. Janzhura, P. Stauning, Magnetic activity in the polar caps: Relation to sudden changes in the solar wind dynamic pressure. *J. Geophys. Res. Sp. Phys.* **112**, 11202 (2007).
22. N. A. Case, J. A. Wild, A statistical comparison of solar wind propagation delays derived from multispacecraft techniques. *J. Geophys. Res. Sp. Phys.* **117**, 2101 (2012).
23. P. Stauning, in *Exploring the Solar Wind* (InTech, 2012; www.intechopen.com).
24. R. J. Carroll, D. Ruppert, L. A. Stefanski, C. M. Crainiceanu, Measurement error in non-linear models: A modern perspective, second edition. *Meas. Error Nonlinear Model. A Mod. Perspect. Second Ed.*, 1–455 (2006).
25. J. W. Gjerloev, The SuperMAG data processing technique. *J. Geophys. Res. Sp. Phys.* **117**, 9213 (2012).
26. P. T. Newell, J. W. Gjerloev, Evaluation of SuperMAG auroral electrojet indices as indicators of substorms and auroral power. *J. Geophys. Res. Sp. Phys.* **116** (2011), doi:10.1029/2011JA016779.

Acknowledgments: We are grateful for the review and feedback from Dr. Kip D Kuntz, Dr. Y. Nishimura, Dr. Stein Haaland, Dr. Ani Chiti, Dr. Katrina Bossert, Dr. Nitin Prasad and Dr. Ying Zou. We also thank Dr. Dogacan Ozturk, Dr. Ryan Dewey, Dr. Banafsheh Ferdousi, and Dr. Jonathon M Smith for fruitful discussions.

Funding:

NASA Cooperative Agreement #80NSSC21M0180G: Partnership for Heliophysics and Space Environment Research (NS)

NASA Heliophysics Participating Investigator Program under Grant #WBS516741.01.24.01.03 (DS)

Author contributions:

Conceptualization: NS, MW, VS

Methodology: NS

Investigation: NS, VS

Formal Analysis: NS, VS

Visualization: NS

Software: NS

Validation: NS, MW

Funding acquisition: DS

Project administration: NS, DS

Supervision: DS, AH, KM

Writing – original draft: NS, VS

Writing – review & editing: NS, VS, DS, MW, KM, AH

Competing interests: Authors declare that they have no competing interests.

Data and materials availability: All data we have used is publicly available. We thank GSFC/SPDF OMNIWeb service for the WIND spacecraft measurements (14). The WIND spacecraft measurements of the solar wind propagated to the bow shock can be accessed from https://spdf.gsfc.nasa.gov/pub/data/omni/high_res_omni/sc_specific/. The polar cap index values PCN and PCS were downloaded from <https://pcindex.org/archive>. We thank Dr. Oleg Troshichev of the Arctic and Antarctic Research Institute for this data (<https://pcindex.org/contacts>). The auroral electrojet indices were downloaded from the SuperMAG database <https://supermag.jhuapl.edu/indices/>. For SuperMAG indices we gratefully acknowledge the SuperMAG collaborators (<https://supermag.jhuapl.edu/info/?page=acknowledgement>). All the relevant data and the MATLAB 2021 codes to process and visualize them have been curated and uploaded in the following GitHub repository <https://github.com/nithinsivadas/uncertainty.git>. For non-MATLAB users the code and its output is accessible as html files.

Supplementary Materials

Materials and Methods

Figs. S1 to S9

References (5–24)

Materials and Methods

Overview

In this section, we discuss the methods used to demonstrate that polar cap potential saturation is a result of solar wind measurement uncertainty, calibrate the error to reveal the linear response of the polar cap potential and auroral current strengths due to solar wind forcing, and present the analytical derivation of uncertainty in measurement times causing a perception of non-linearity in a linear system's correlation response.

Solar wind measurement uncertainty

Solar wind interaction with the Earth's magnetosphere causes day-side magnetic reconnection that drives the convection of magnetic fields and plasma in the Earth's polar ionosphere. The upper limit of the rate of the magnetic reconnection is determined by the solar wind reconnection electric field or merging geoeffective field E_m (5).

$$E_m = V_{sw} B_{T,sw} \sin^2(\theta_{sw}/2) \quad [1.1]$$

This field is determined by solar wind parameters alone and is also known as the Kan-Lee electric field (15). Here V_{sw} is the solar wind speed in km/s, $B_{T,sw} = \sqrt{B_y^2 + B_z^2}$ is the transverse magnitude of the interplanetary magnetic field (IMF) in nT, and $\theta_{sw} = \tan^{-1}(B_y/B_z)$ is the transverse IMF clock angle in radians. E_m is a positive-valued quantity with the units of the electric field [mV/m], reflecting the assumption that energy flows only from the solar wind to the magnetosphere. The above quantities are measured in Geocentric Solar Magnetospheric (GSM) coordinates using spacecrafts orbiting the L1 libration point ~ 230 earth Radii (R_E) upstream from Earth. The GSM coordinates are convenient for studying the effects of the IMF components on magnetospheric and ionospheric phenomena. Its X-axis points towards the Sun, and the Z-axis is the projection of the Earth's magnetic dipole axis onto the plane perpendicular to the X-axis. For purely southward IMF, the reconnection electric field E_m is equal to the solar wind electric field $E_{sw} = V_{x,sw} B_z$, where $V_{x,sw}$ is a component of the solar wind velocity along the x-direction.

The dawn-dusk portion of the solar wind electric field maps along the equipotential magnetic field lines and drives the plasma convection down in the polar cap ionosphere. The convection corresponds to an electric field across the polar cap in the rest frame of the Earth (E_{PC}). The polar cap (PC) index is a measure of this field and the energy input into the Earth's magnetosphere. The index has gone through many iterations over the past 50 years, but it is essentially the maximum amplitude of variations observed from magnetometers within the polar cap (6). The current version of the index is scaled on a statistical basis of magnetic variations to the reconnection electric field. This makes the PC index independent of daily and seasonal variations and the local ionospheric properties. PCN is the index derived from magnetometer arrays in the northern polar cap, while PCS is derived from the southern polar cap. We use the PCC index as a proxy for E_{PC} , as it combines both the indices to provide a positive-valued index, which is more accurate than the individual indices (6). PCC or E_{PC} also has the units of the electric field, and it is mostly represented in literature in the form of its corresponding electric potential across the polar cap, called the cross-polar cap potential.

When E_m is propagated to the polar cap ionosphere from the L1 point (\hat{E}_m), it correlates linearly with E_{PC} for low values of \hat{E}_m . This is well-documented in literature and is observed for

other forms of the solar wind electric field and polar cap index (5, 6, 16). However, we note that the true value of \hat{E}_m is unavailable to us, as there will always be some inherent errors in the propagation model. Instead, we only have an erroneous estimate of the reconnection electric field propagated to the polar cap – \hat{E}_m^* . Hence, we need to reinterpret the literature as saying that low values of the erroneous estimate of the solar wind strengths \hat{E}_m^* (not \hat{E}_m) correlate linearly with the polar cap potential. And at high values of \hat{E}_m^* , the polar cap potential saturates. The saturation seems to have the following functional form (6):

$$E_{PC} = \frac{\hat{E}_m^*}{\sqrt{1 + (\hat{E}_m^*/E_0)^2}}$$

We calculate \hat{E}_m^* by using WIND satellite measurements published in the OMNIWeb database (17). The database provides the values corrected for the propagation delay of the solar wind from L1 to the bow-shock nose (18–20). Then as commonly done, we apply a further correction of a constant delay of ~20 minutes to account for the propagation delay from the nose to the polar cap ionosphere (21). Previous literature that discusses the polar cap potential saturation problem estimates \hat{E}_m^* similarly. We use the WIND data from 1995 to 2019 and the polar cap indices from the same time range. Both data are 1-minute averages. We only use data samples when both WIND measurements and polar cap indices are available.

We categorize the uncertainty in estimating \hat{E}_m^* into three primary sources:

1. Uncertainty in propagation delay of the solar wind from L1 to the bow-shock nose (dt_1)
2. Uncertainty in the propagation delay of the effect of solar wind forcing from bow-shock noses to the polar cap ionosphere (dt_2)
3. Random variability in the magnitude of E_m due to spatial variation in the solar wind and changes in other environmental parameters such as ionospheric conductivity (ε)

Knowing the statistical distribution of the above uncertainty will allow us to construct a stochastic model of the estimate \hat{E}_m^* as a function of the accurate value \hat{E}_m mapped to the polar cap ionosphere. In the following subsection, we develop a statistical error model of the estimate of the reconnection electric field in the polar cap ionosphere from the hypothetical true value and uncertainty distributions. For the assumed uncertainties, the model predicts the polar cap potential saturation that is strikingly similar to data from 20 years of observations (see Fig. 2).

Statistical error model

To distinguish between data and model, we will replace E_m with X when referring to the random variable corresponding to the reconnection electric field in the statistical model. We also replace the polar cap index E_{PC} with a counterpart in the model X_{PC} . Hence, in the model, \hat{X} is the value of the reconnection electric field accurately propagated to the polar cap, and \hat{X}^* is its erroneous estimate. We hypothesize the following statistical error model:

$$\hat{X}^*(t) = \hat{X}(t + dt_1 + dt_2) + \varepsilon(t) \quad [1.2]$$

We assume that \hat{X}^* , \hat{X} , dt_1 , dt_2 , and ε are stochastic processes. In other words, they are each a collection of random variables in time ($t \in T$) with an associated probability distribution

that determines the random value it might take at a given time t . Below we present the justified assumptions we make of the probability distributions and autocorrelation functions of these stochastic processes. From these assumptions of \hat{X} , dt_1 , dt_2 , and ε , we calculate \hat{X}^* . After which, we validate the model results by comparing them with the data \hat{E}_m^* .

Input \hat{X} : As discussed earlier, accurate mapping of the reconnection electric field onto the polar cap should result in $\hat{X}=X_{PC}$. As a result, we assume that the probability density function (pdf) of \hat{X} is similar to the pdf of X_{PC} , hence the pdf of E_{PC} that we can estimate from data. Like many solar wind parameters, E_{PC} can be approximated to be a lognormal distribution (8). Without making any specific equivalence, we assume the pdf of model input \hat{X} to be a lognormal distribution that closely fits the pdf of E_{PC} from data (See fig. S1). We also assume the adjacent values of \hat{X} in time are correlated similarly to adjacent values of E_{PC} in time (See fig. S2). In other words, we assume that in our model, \hat{X} shares the stochastic properties of the polar cap index E_{PC} . Finally, we assume \hat{X} is a stationary process, i.e., its probability distribution and autocorrelation function does not change with time.

Uncertainty in propagation delay from L1 to Nose dt_1 : Solar wind parameters measured upstream are time-shifted to account for the delay in propagation of the wind to the bow-shock nose. Case and Wild estimate the uncertainty to be on the order of minutes (22). Based on their results, we assume dt_1 to be an independent random process with a pdf of a Student's t-distribution with shape factor 1.3, mean 0, and standard deviation 8 minutes (See Fig. S3). The distribution is zero-mean and has a longer tail than the normal distribution.

Uncertainty in propagation delay from nose to polar cap dt_2 : Changes in the day-side reconnection electric field propagate along equipotential magnetic field lines to the polar caps. The delay in this propagation is on average 20 minutes but can vary from -5 to 50 minutes (23). Historically, researchers have used a constant propagation delay (t_2) of about 20 minutes for this stage of propagation. However, the uncertainty of propagation time here is significant. We model the pdf of t_2 as a Weibull distribution with mean zero, standard deviation 25 minutes, and shape factor 1.3 (See fig. S3). The Weibull distribution keeps the total delay $t_2 + dt_2$ positive and captures the broad spread in the propagation delay documented by Stauning (23).

Other uncertainty ε : There are several other reasons for the magnitude of the solar wind electric field to be different from where it is measured at the L1 and its projection at the polar cap. The IMF clock angle could change substantially after crossing L1, spatial variations in the solar wind can lead to a different part of the wind interacting with the Earth's magnetosphere, and changes in ionospheric conductivity, or more generally, the magnetospheric state can lead to changes in the electric field value at the polar cap. As the solar wind strength increases, the random variation in the field can increase due to the increased spatial structuring of the solar wind. With more energy in the magnetosphere affecting particle precipitation, a larger range of ionospheric conductance values is possible for given solar wind strength. However, beyond a threshold, large solar wind structures with uniform spatial scales, like Coronal Mass Ejections, might lead to a lower increase in random variation with solar wind strength.

Though we do not use direct evidence, the above assumption is consistent with the observed statistical variations in the difference between solar wind electric field and the polar cap potential shown in fig. S7. The variation in their difference increases up to a polar cap potential of ~ 12 mV/m and then remains constant. Hence, the normalized variation shown in fig. S7 (spread of

points across the horizontal direction) decreases after ~ 12 mV/m. Based on this observation, we model the pdf of ε to be a zero-mean Gaussian, but with a standard deviation that varies with the magnitude of \hat{X} . The specific function that we assume for the standard deviation of ε normalized by the value of \hat{X} is shown in fig. S4. The normalized standard deviation of ε in fig. S4 increases up to 12 mV/m and then decreases slowly after. We also assume that ε has an autocorrelation function similar to that of the difference between the observed reconnection electric field \hat{E}_m^* and the polar cap index E_{PC} .

Using the above assumptions, we generate an ensemble of time series of \hat{X} , dt_1 , dt_2 , and ε , and calculate the corresponding time series of the erroneous estimate \hat{X}^* using equation [1.2]. The statistical properties of the model output agree remarkably with that of the data.

Model validation

1. The model predicts the pdf of the erroneous estimate of the reconnection electric field \hat{E}_m^* . As shown in fig. S5, the pdf of \hat{X}^* closely fits the pdf of \hat{E}_m^* .
2. The model predicts the standard deviation of the normalized error. A good way to visualize how the uncertainty varies with the magnitude of \hat{X}^* is to calculate the standard deviation of the normalized error $\sum (\hat{X}^* - \hat{X})/\hat{X}$. This quantity largely matches with its counterpart in data $\sum (\hat{E}_m^* - E_{PC})/E_{PC}$ (See fig. S6). If the values we assume for the uncertainties dt_1 , dt_2 , and ε , are inadequate, the model will underestimate or overestimate the statistical variation in the difference between \hat{E}_m^* and E_{PC} shown in fig. S6.
3. Furthermore, the model predicts the conditional normalized error distribution itself. A more detailed picture of the statistical properties of \hat{E}_m^* can be obtained by plotting the conditional probability density of the normalized error given \hat{X} or E_{PC} . In fig. S7, the left plot is the conditional pdf of normalized error calculated from the data, and the plot on the right is the same from the model. Both have a similar structure, with the spread in error increasing up to ~ 12 mV/m and then decreasing. This is consistent with our assumptions of the variation of the spatial scale sizes with solar wind strength.
4. Finally, the model shows that the assumptions of random, unbiased uncertainties in the solar wind input lead to a conditional bias in the estimate \hat{X}^* varying with its strength. This bias exactly reproduces that seen in the data. In fig. S8, the black line is plotted from data and shows the conditional bias in the erroneous estimate \hat{E}_m^* given its strength. It matches remarkably with that calculated by the model – shown in magenta. This non-linearly increasing bias is ultimately a result of the regression to the mean effect and regression attenuation (9, 24).

Fig. S9 visualizes this effect. The left panel shows the probability distribution of the true value \hat{X} . Each bin associated with \hat{X} is assigned a unique color. The panel on the right shows the pdf of the error-prone estimate of \hat{X} , i.e., \hat{X}^* . However, the colors still preserve their correspondence to the true value. The share of color in a particular \hat{X}^* bin describes the proportion of \hat{X} values misidentified as \hat{X}^* . In each \hat{X}^* bin, a larger proportion of lower \hat{X} values

are misidentified as \hat{X}^* . In other words, for large \hat{X}^* , \hat{X} is less than expected. Converting this into the terminology of observations, we get back to the statement of the problem introduced in the main paper: for large values of \hat{E}_m^* , E_{PC} is less than expected or *saturates*.

Correcting the error

From the model output, we calculate the conditional expectation of the true value given the erroneous estimate: $f_r(x) = \langle X|X^* = x \rangle$. For the particular assumptions of uncertainties in measurement, $f_r(x)$ is the best estimate of the true value given the erroneous value. $f_r(x)$ can be used to statistically correct the erroneous estimate \hat{E}_m^* to a most likely estimate of the true value \hat{E}_m^c . \hat{E}_m^c is useful for revealing the true statistical correlation with other variables, like the polar cap index E_{PC} or auroral current strengths SML . The process of statistically correcting for the uncertainty using the conditional expectation of the true value given the erroneous estimate: $\hat{E}_m^c = f_r(\hat{E}_m^*)$ for accurate regression analysis is called regression calibration (24). Fig. 3 shows the results of this calibration. SML is the lower auroral electrojet index from the SuperMAG database, which is a measure of the currents flowing in the auroral regions (25, 26). It is calculated using ground magnetometers and procedures completely independent of the calculation of the polar cap index. Since regression calibration of \hat{E}_m^* to \hat{E}_m^c , results in a linear relationship between both \hat{E}_m^c and E_{PC} (Fig. 3A) and \hat{E}_m^c and SML (Fig. 3A), it suggests our findings are independent of the construction of the ionospheric response variables.

Temporal uncertainty can lead to a non-linear regression function

Here we analytical derive the general result that temporal uncertainty in measurement can lead to a perception of non-linearity in a linear system's correlation response. For this, we first assume a linear system with an input random variable X and output response variable Y , such that

$$Y = X \quad [1.3]$$

The input is measured or estimated with a temporal uncertainty represented by the random variable Δ . The erroneous estimate is W and is related to the true input X as

$$W = X(t + \Delta) \quad [1.4]$$

where the statistics of X and Δ are known

$$X \sim f_X(x)$$

$$\Delta \sim f_\Delta(\delta)$$

Our goal here is to find the erroneous regression function $\langle Y|W \rangle = f_r^*(w)$ and see how different it is from the true regression function $\langle Y|X \rangle$. Based on equation [1.3], $\langle Y|X \rangle$ is simply $f_r(x) = x$. We also note that since the system has a simple linear response $\langle Y|W \rangle = \langle X|W \rangle = f_r^*(w)$. For the rest of the section, our goal is to derive the function $\langle X|W \rangle$ or $f_r^*(w)$.

Firstly, we note that since $W(t)$ is a stochastic process, from equation [1.4], the conditional distribution

$$f_{W|\Delta}(w|\Delta = \delta) = f_{X(t+\delta)}(w)$$

But since X is assumed to be a stationary process,

$$\begin{aligned} f_X(w) &= f_{X(t+\delta)}(w) \\ \Rightarrow f_{W|\Delta}(w|\Delta = \delta) &= f_X(w) \end{aligned} \quad [1.5]$$

However,

$$\begin{aligned} f_W(w) &= \int f_{W,\Delta}(w, \delta) d\delta \\ &= \int f_{W|\Delta}(w|\Delta = \delta) f_{\Delta}(\delta) d\delta \end{aligned} \quad [1.6]$$

And from equation [1.6],

$$f_W(w) = \int f_X(w) f_{\Delta}(\delta) d\delta$$

As we assume X and Δ are independent, and $\int f_{\Delta}(\delta) d\delta = 1$, hence

$$f_W(w) = f_X(w) \quad [1.7]$$

That is, **the marginal distribution of W and X has the same functional form.**

From equations [1.5] and [1.7], it follows that **W and Δ are also independent.**

$$\begin{aligned} f_{W,\Delta}(w, \delta) &= f_{W|\Delta}(w|\delta) f_{\Delta}(\delta) \\ &= f_X(w) f_{\Delta}(\delta) \\ &= f_W(w) f_{\Delta}(\delta) \end{aligned} \quad [1.8]$$

Now we estimate the joint probability distribution function of W , X , and Δ .

$$f_{W,X,\Delta}(w, x, \delta) = f_{W|X,\Delta}(w|x, \delta) f_{X,\Delta}(x, \delta)$$

Since X and Δ are independent,

$$f_{W,X,\Delta}(w, x, \delta) = f_{W|X,\Delta}(w|x, \delta) f_X(x) f_{\Delta}(\delta) \quad [1.9]$$

By integrating the above over the range of Δ , we can calculate the marginal pdf of W and X .

$$f_{W,X}(w, x) = \int f_{W|X,\Delta}(w|x, \delta) f_X(x) f_{\Delta}(\delta) d\delta \quad [1.10]$$

Finally, we can calculate the conditional pdf of X given W .

$$f_{X|W}(x|w) = \frac{f_{W,X}(w,x)}{f_W(w)}$$

From equation [1.7], we see that

$$f_{X|W}(x|w) = \frac{f_{W,X}(w,x)}{f_X(w)}$$

Using this and equation [1.10], we get

$$f_{X|W}(x|w) = \int f_{W|X,\Delta}(w|x, \delta) \frac{f_X(x)}{f_X(w)} f_{\Delta}(\delta) d\delta \quad [1.11]$$

Hence from the definition of expectations we get,

$$\langle X|W \rangle = f_r^*(w) = \int x f_{X|W}(x|W = w) dx \quad [1.12]$$

To solve equation [1.12], we need to assume a functional form for the pdf of X and Δ . $f_X(x)$ is assumed to be lognormal distribution, and $f_\Delta(\delta)$ to be a normal distribution. A lognormal random variable X has a corresponding normally-distributed random variable Z such that

$$\begin{aligned} Z &\sim \phi(z, \mu_Z, \sigma_Z) \\ Z &= \log X \\ \mu_Z &= \log \left(\frac{\mu_X^2}{\sqrt{\mu_X^2 + \sigma_X^2}} \right) \\ \sigma_Z &= \sqrt{\log \left(1 + \frac{\sigma_X^2}{\mu_X^2} \right)} \end{aligned} \quad [1.13]$$

Here, the function ϕ is the general normal distribution.

$$\phi(x, \mu, \sigma) = \frac{1}{\sqrt{2\pi}\sigma} e^{-\frac{(x-\mu)^2}{2\sigma^2}} \quad [1.14]$$

Therefore,

$$f_X(x) = \frac{1}{x} \phi(\log x, \mu_Z, \sigma_Z) \quad [1.15]$$

Additionally, as $X(t)$ is a stochastic process, the random variable at each time instance correlates to some degree with adjacent time instances. We define this using an autocorrelation function of the following form

$$\rho_X(\delta, k) = e^{-\delta/k} \quad [1.16]$$

Here $\delta = |t_2 - t_1|$ is the absolute difference in time between two random variables, $X(t_2)$ and $X(t_1)$. For our case, this is also the error in measurement time corresponding to $\Delta \sim f_\Delta(\delta)$. k is the **autocorrelation time constant**.

The normally distributed uncertainty in time is defined as

$$f_\Delta(\delta) = \phi(\delta, 0, \sigma_\delta) \quad [1.17]$$

Here σ_δ is a **measure of the random uncertainty in the time of measurement Δ** .

From equations [1.13] and [1.16], we can estimate the autocorrelation function corresponding to the normal random variable Z

$$\rho_Z(\delta, k) = \frac{1}{\sigma_Z^2} \log(1 + \rho_X(\delta, k) [e^{\sigma_Z^2} - 1]) \quad [1.18]$$

From the results of the bivariate lognormal distribution, we can derive the functional form of $f_{W|X,\Delta}(w|x, \delta)$ to be the following

$$f_{W|X,\Delta}(w|x, \delta) = \frac{1}{w} \phi \left(\log w, \mu_Z + \rho_Z(\delta, k)[\log x - \mu_Z], \sigma_Z \sqrt{1 - \rho_Z(\delta, k)^2} \right) \quad [1.19]$$

From equations [1.11],[1.12],[1.15],[1.17], and [1.19], we can calculate the regression function $\langle X|W \rangle = f_r^*(w)$.

$$f_r^*(w) = \int_0^{\infty} \int_{-\infty}^{\infty} \phi \left(\log w, \mu_Z + \rho_Z(\delta, k)[\log x - \mu_Z], \sigma_Z \sqrt{1 - \rho_Z(\delta, k)^2} \right) \frac{\phi(\log x, \mu_Z, \sigma_Z)}{\phi(\log w, \mu_Z, \sigma_Z)} \phi(\delta, 0, \sigma_\delta) d\delta dx \quad [1.20]$$

By integrating the above integral within the ranges of x , and substituting $\frac{\delta}{k} \rightarrow u$, we can show that the above integral is a function of the ratio $\frac{\sigma_\delta}{k}$. This ratio as a measure of uncertainty in the time of measurement.

$$f_r^* \left(w, \frac{\sigma_\delta}{k} \right) = \int_{-\infty}^{\infty} w^{\rho_Z(u)} e^{\frac{1}{2}[1-\rho_Z(u)][2m_Z+(1+\rho_Z(u))\sigma_Z^2]} \frac{1}{\sqrt{2\pi} (\sigma_\delta/k)} e^{-\frac{u^2}{2(\sigma_\delta/k)^2}} du \quad \text{where } u = \delta/k$$

We numerically integrate the above integral within the ranges of Δ for specific values of σ_δ/k and generate Fig. 4. The pdf of X is the same as that assumed for \hat{X} in the previous section, with the mean $\mu_X = 1.15$ and standard deviation $\sigma_X = 1.14$. The figure shows that $f_r^*(w, \sigma_\delta/k)$ varies non-linearly with w when the temporal uncertainty ratio is larger than 0%, compared to $f_r(x) = x$ (which is linear) when $W = X$ or the temporal uncertainty ratio is 0%. Therefore, we have found that the regression function $\langle Y|W \rangle = f_r^*(w, \sigma_\delta/k)$ is non-linear with respect to w for values of $\sigma_\delta/k > 0$.

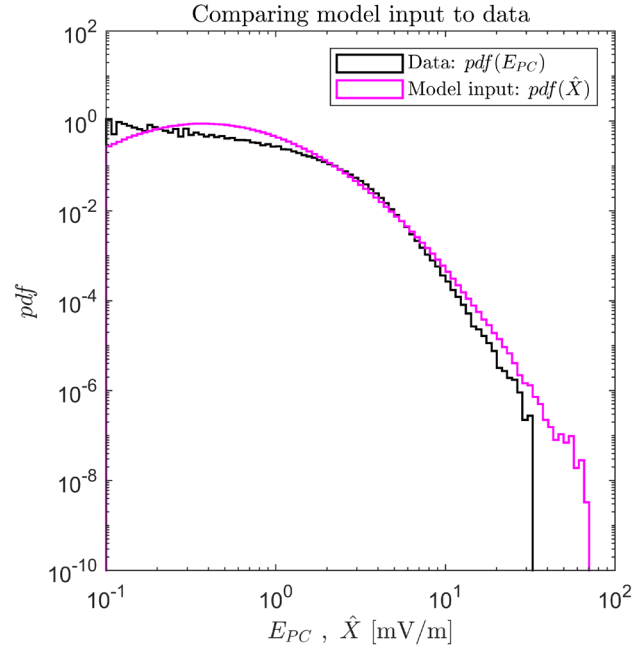


Fig. S1. The black line shows the pdf of the polar cap index E_{PC} from 1995 to 2019. And the magenta line shows the lognormal pdf of the model random variable \hat{X} that best fits the pdf of E_{PC} .

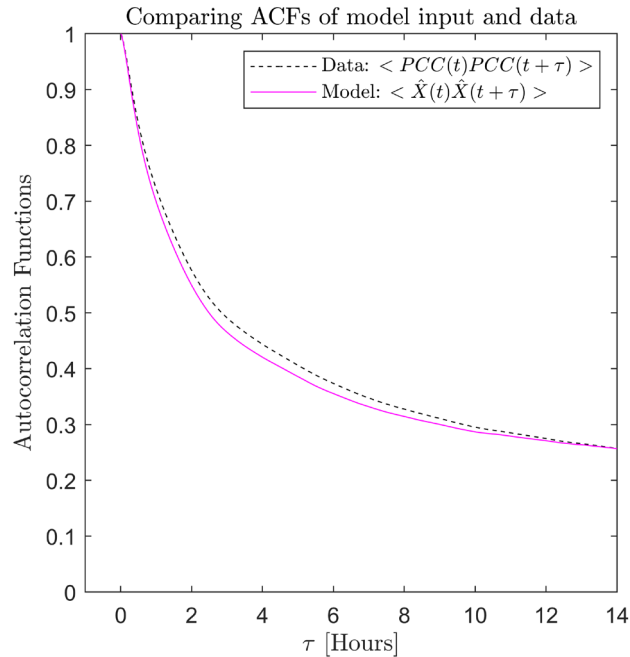


Fig. S2. The black dashed line shows the autocorrelation function of the polar cap index E_{PC} averaged over data from 1995 to 2019. And the magenta line shows the autocorrelation function of the model random variable \hat{X} that closely follows the ACF of E_{PC} .

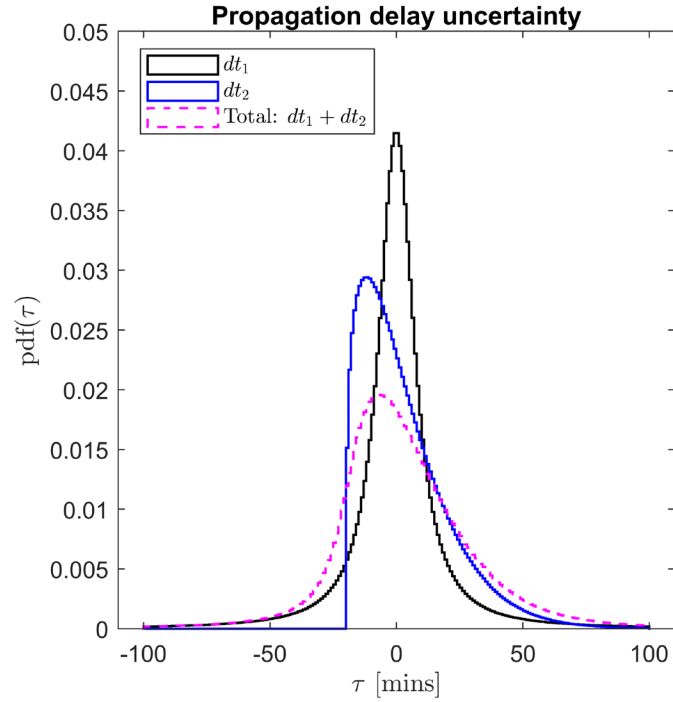


Fig. S3. The black line shows the uncertainty in the propagation delay from L1 to the bow shock nose(dt_1). The blue line shows the uncertainty in the propagation delay from the bow-shock nose to the polar cap ionosphere(dt_2). The magenta line shows the total uncertainty in the propagation delay from L1 to the polar cap($dt_1 + dt_2$).

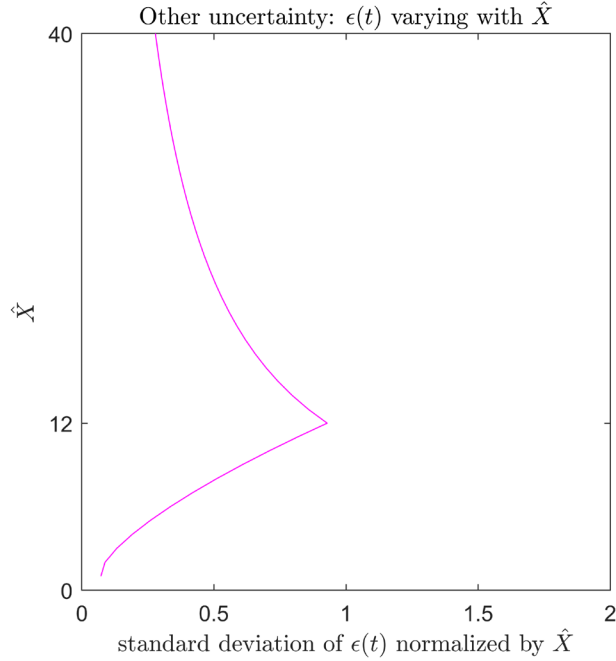


Fig. S4. The uncertainty ε normalized with the magnitude of \hat{X} in the stochastic model increases up to 12 mV/m and slowly diminishes with increasing \hat{X} beyond that point. This is consistent with the measurements of the difference between \hat{E}_m^* and E_{PC} in Fig. S7.

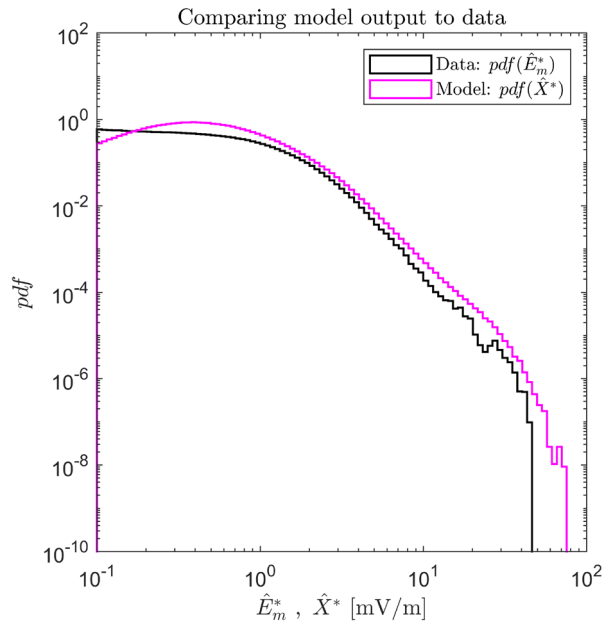


Fig. S5. The model predicts the pdf of the estimate of the merging electric field propagated to the polar cap, almost exactly. \hat{E}_m^* is data, and \hat{X}^* is model.

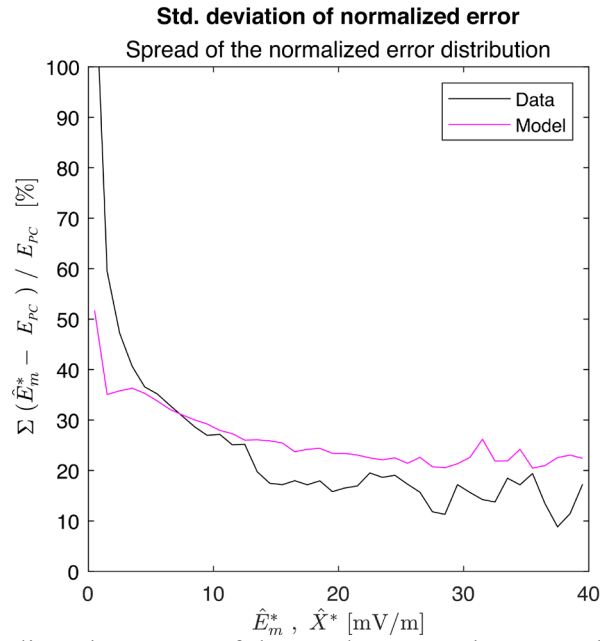


Fig. S6. The model predicts the nature of the random error between the estimate and the true value of the merging electric field projected on the ionosphere. The black line is the normalized uncertainty associated with \hat{E}_m^* (data), and the purple line is the normalized uncertainty associated with \hat{X}^* (model).

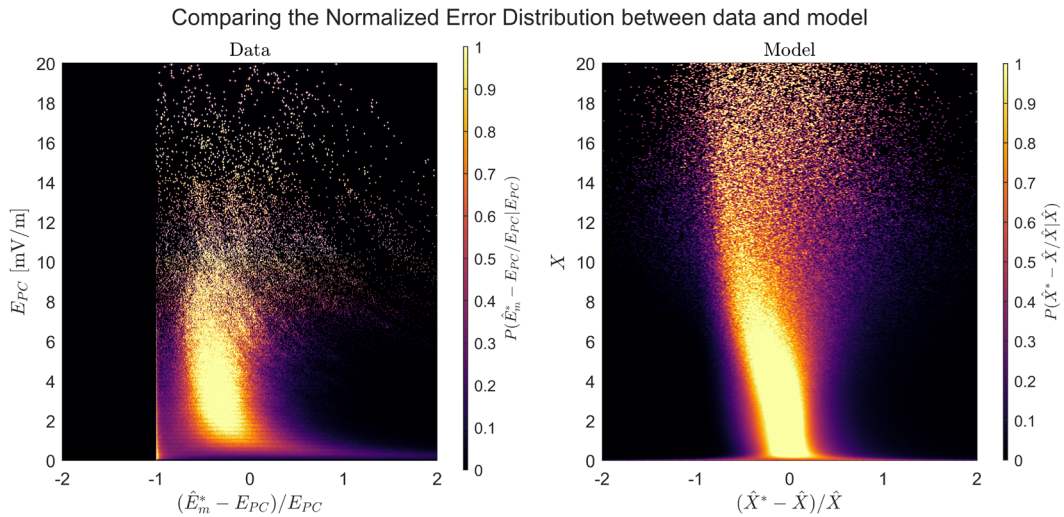


Fig. S7. (Left) Conditional normalized error distribution from data, (Right) Conditional normalized error distribution from the model. Both show similar trends in how the error varies with increasing strength of the true variable –a steep increase in the spread of the error from 0 to ~12 mV/m in the vertical axis, and then a decrease beyond that point.

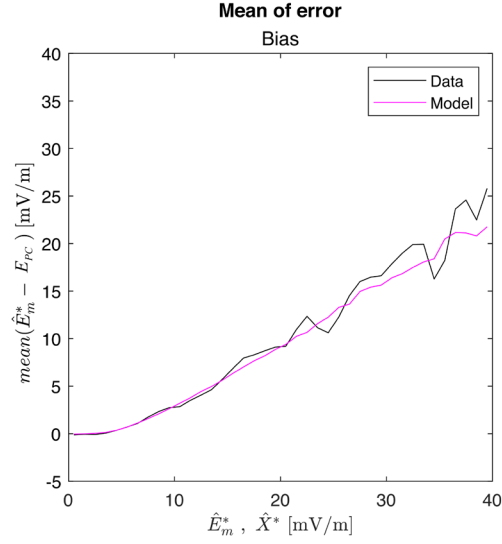


Fig. S8. There is a non-linear conditional bias in \hat{E}_m^* : $\langle \hat{E}_m^* - E_{PC} | E_{PC} \rangle$ that varies with E_{PC} , which is reproduced very well by the model $\langle \hat{X}^* - \hat{X} | \hat{X} \rangle$.

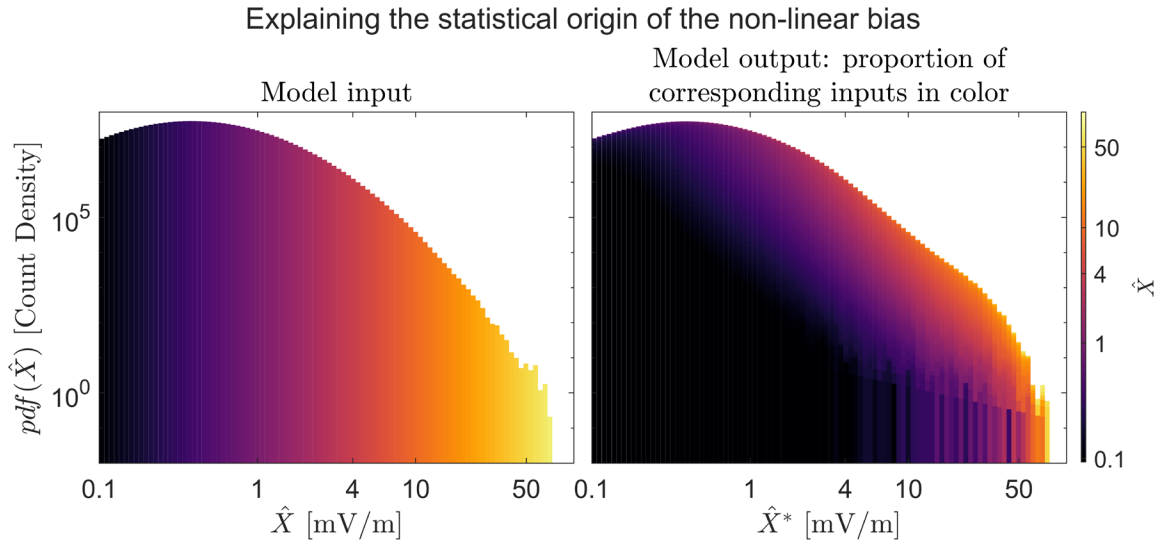


Fig. S9. (Left) Probability distribution function of the true variable \hat{X} , with each bin colored uniquely. (Right) The probability distribution function of the inaccurate estimate of \hat{X} , i.e., \hat{X}^* with the color representing the magnitude of \hat{X} . The amount of a particular color per bin represents the proportion of \hat{X} values misidentified as \hat{X}^* .